Catalysis Science & Technology

ROYAL SOCIETY OF CHEMISTRY

PAPER

View Article Online
View Journal | View Issue

Cite this: *Catal. Sci. Technol.*, 2025, **15**, 1814

Oxygen vacancy-engineered In_2O_3@carbon catalysts from steam-pyrolyzed MOFs for photothermal CO_2 hydrogenation†

Xinhuilan Wang,‡ Luis Garzon-Tovar,‡ Alejandra Rendón-Patiño, Diego Mateo * and Jorge Gascon *

Received 18th December 2024,
Accepted 3rd February 2025

DOI: 10.1039/d4cy01515k

rsc.li/catalysis

Photothermal CO_2 hydrogenation has attracted considerable attention as a promising approach to utilize carbon dioxide through the efficient conversion of solar energy into chemicals and fuels. In this study, we report a novel approach to improve the catalytic performance of indium oxide-based catalysts for the photothermal reverse water-gas shift (RWGS) reaction. Catalysts derived from the steam pyrolysis of the metal–organic framework MIL(In)-68 display a high density of oxygen vacancies and defect sites on the In_2O_3 surface. These features significantly enhance CO_2 adsorption and H_2 dissociation ability while maintaining the porosity of the material and enhancing its photothermal properties. Among the catalysts investigated, the Rb-promoted catalyst exhibited superior activity, achieving CO production rates of 53 mmol $g_{In_2O_3}^{-1}$ h^{-1} with 100% selectivity without any external heating. Comprehensive characterization, including XPS and Raman spectroscopy, confirmed that steam-pyrolysis leads to extensive defective site formation, resulting in improved catalytic performance. These results highlight the potential of steam-pyrolyzed MOF materials as efficient and selective catalysts for photothermal CO_2 hydrogenation, offering a sustainable route to valuable chemical production.

1. Introduction

The global rise in CO_2 emissions presents a critical challenge for environmental sustainability and climate change mitigation.[1,2] The pursuit of carbon neutralization is driving a transition from fossil fuels to renewable energy sources integrated with CO_2 recycling.[3,4] Among these strategies, CO_2 hydrogenation stands out as a promising approach for converting CO_2 into value-added chemicals[5,6] and fuels,[7] thereby advancing carbon capture and utilization (CCU).[8,9] However, most of the current catalytic pathways for CO_2 valorization rely on high temperatures and thermal energy typically derived from the combustion of non-renewable resources.[10,11] This dependence on fossil fuels not only undermines the overall sustainability of the process but also limits the net reduction of CO_2 emissions, posing a significant challenge to achieve carbon neutrality.

Recently, photothermal catalysis, which leverages the synergistic combination of thermal and non-thermal energy, has gained significant attention as a way to drive chemical reactions by efficiently utilizing the entire solar spectrum, particularly the visible and near-infrared regions.[12] This approach integrates thermochemistry and photochemistry into a single process, overcoming the energy constraints and poor catalytic performances typically associated with conventional thermal catalysis and purely photocatalytic systems, respectively. By harnessing both light and thermal energy, photothermal catalysis enhances catalytic efficiency through improved light absorption and thermal activation. On the one hand, elevated temperatures not only improve reaction kinetics, but also increase the probability to overcome the reaction energy barriers, thus facilitating higher reaction rates. Additionally, photonic energy can activate adsorbed species or decrease the energy requirements of certain reaction steps, significantly boosting catalytic activity. As a result, photothermal catalysis has shown considerable potential in the production of solar fuels and chemicals, such as methane,[13–15] methanol[16] and carbon monoxide[17,18] through CO_2 hydrogenation.

Recent developments in photothermal CO_2 hydrogenation have highlighted indium oxide (In_2O_3) and In_2O_3-supported solids as outstanding catalysts. The role of oxygen vacancies in In_2O_3 is particularly significant, facilitating CO_2 activation[19,20] and narrowing the bandgap for enhanced light absorption.[21] For instance, Ye and coworkers have demonstrated that the 2D

Advanced Catalytic Materials (ACM), KAUST Catalysis Center (KCC), King Abdullah University of Science and Technology (KAUST), Thuwal 23955-6900, Saudi Arabia. E-mail: diego.mateo@kaust.edu.sa, jorge.gascon@kaust.edu.sa

† Electronic supplementary information (ESI) available. See DOI: https://doi.org/10.1039/d4cy01515k

‡ These authors contributed equally to this work.

black In_2O_{3-x} nanosheets with bifunctional oxygen vacancies[19] and carbon-doped In_2O_3 with dense oxygen vacancy[20] could provide efficient local heat generation and improve the CO_2 adsorption ability. In a related work, Ozin *et al.*[21] investigated the formation of oxygen vacancies on indium oxide through a pre-treatment with hydrogen at high temperatures, facilitating an outstanding CO productivity compared to pristine In_2O_3. These findings underscore the importance of developing novel indium-based catalysts with enhanced defect sites to improve photothermal properties. In addition to indium-based structures, carbon-based materials derived from the controlled pyrolysis of metal–organic frameworks (MOFs) also represent an interesting family of materials with huge potential as photothermal catalysts.[22–26] Our group previously proposed the use of steam during the pyrolysis process (from now on, steam-pyrolysis) as a novel approach for controlling the phases and properties of MOF-derived catalysts.[27] By introducing water during pyrolysis, Khan and co-workers successfully controlled the partial oxidation process, promoting stable metal oxides while preventing carbide formation. Interestingly, this approach also results in smaller particle sizes and tunable active phases. Overall, these findings demonstrate that steam-pyrolyzed materials can be highly efficient for catalytic processes such as CO_2 hydrogenation where phase control and particle size are critical.

In this work, we present the combination of oxygen vacancy-enriched In_2O_3 structures together with MOF-derived materials as a strategy to obtain effective and selective catalysts for the photothermal RWGS reaction. In particular, we have explored the introduction of steam during the pyrolysis process of MIL(In)-68 MOF to create an indium oxide@carbon heterostructure with enhanced defective sites on the In_2O_3 surface (Scheme 1). Among all the catalysts, the Rb-promoted In@C-25 catalyst demonstrated the highest catalytic activity, achieving production rates of 53 mmol $g_{In_2O_3}^{-1}$ h^{-1} with a 100% CO selectivity in the absence of any external heating, to the best of our knowledge, a new benchmark for the photo-thermal CO_2 hydrogenation using In_2O_3-based catalysts. XPS, Raman and N_2-adsorption measurements revealed that the steam-pyrolysis process could induce abundant defect sites on the In_2O_3 catalyst, improving CO_2 adsorption capacity and H_2 dissociation ability while maintaining enriched porosity. Moreover, mechanistic studies suggested that the reaction mechanism is dominated by non-thermal effects, particularly at high irradiances, in combination with pure thermal contributions.

2. Materials and methods

2.1. Catalyst synthesis

Synthesis of MIL-68(In). MIL-68(In) MOF was prepared in a similar manner as in ref. 28 and 29 with small modifications. In short, 1.05 mmol of $In(NO_3)_3{\cdot}H_2O$ (Thermo Scientific, 99.99%) and 1.2 mmol of 1,4-benzenedicarboxylic acid (Sigma Aldrich, 99.9%) were dissolved in 12.4 mL of DMF in a 30 mL glass vial. After 30 minutes of stirring, the sealed glass vial was maintained at 100 °C for 48 hours. The product was collected by centrifugation, washed three times with 30 mL DMF and three times with 30 mL ethanol, and finally dried in a vacuum oven overnight at 60 °C.

Synthesis of In@C sample by pyrolysis. The as-synthesized MIL-68(In) sample was conducted in a quartz tubular reactor vertically placed in a tube furnace. In a typical experiment, MOF powder was placed in the reactor under continuous N_2 flow (25 mL min^{-1}) at 600 °C for 6 hours using a heating ramp of 2 °C min^{-1}. After cooling down of the reactor, the samples were passivated in a continuous flow of oxygen (5 mL min^{-1}) for 2 h to fabricate the In@C sample.

Synthesis of In@C-*X* sample by steam-pyrolysis. In a typical experiment, a water bubbler was connected to a nitrogen line. The water content was controlled by varying the temperature of the water cooler connected to the bubbler

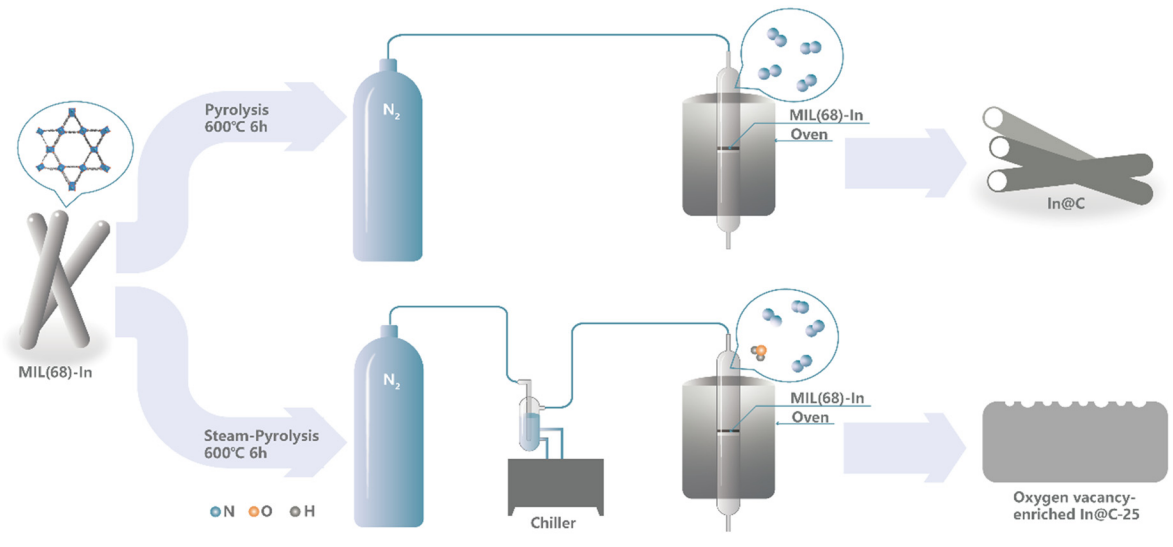

Scheme 1 Schematic illustration of the steam-pyrolysis and pyrolysis process.

(5, 25, and 40 °C).[27] The as-synthesized MIL-68(In) sample was conducted in a quartz tubular reactor vertically placed in a tube furnace under a continuous wet nitrogen flow (25 mL min^{-1}) at 600 °C for 6 hours. After cooling down, In@C-*X* (*X* = 5, 25, and 40 for different temperatures of bubbler) sample was obtained.

Wet impregnation of In@C and In@C-*X* catalysts. In@C and In@C-*X* samples were impregnated with a solution of different metal nitrate in water by incipient wetness impregnation to obtain 2 wt%. In a typical procedure, 3.45 mg $Rb(NO_3)_2$ was dissolved in 60 μL deionized water and added into 100 mg In@C sample drop by drop. Subsequently, a Rb-promoted In@C sample was obtained after drying at 80 °C for 2 hours. The procedure was repeated for the remaining promoters explored in this study (K and Cs).

2.2. Photo-thermal experiments

The photo-thermal reverse water gas shift reaction (RWGS) was evaluated using a commercial flow reactor equipped with a quartz window (Harrick, HVC-MRA-5) and a 300 W Xe lamp (PE300BFA, Perfectlight) as the irradiation source. In a typical experiment, 30 mg of catalyst was loaded on the reactor. A thermocouple to monitor the temperature was located *ca.* 1 mm below the catalyst's surface. The reaction gas mixture (H_2/CO_2 molar ratio of 4 : 1) was introduced through the reactor with a total flow rate of 10 mL min^{-1} (GSHV = 20 000 mL h^{-1} g^{-1}). Nitrogen was used as an internal standard. The outlet of the reactor was directly connected to the inlet of the gas chromatograph (SRA instruments) equipped with two modules and a TCD detector to determine the concentration of gases. One of the modules has a MS5A column and analyses H_2, CH_4, and CO using Ar as carrier gas. The second module has a PPU column and analyses CO_2 and up to C_{2+} hydrocarbons using He as carrier gas.

CO formation rate calculations were normalized by the In_2O_3 content. CO_2 conversion (X_{CO_2}, %) and CO selectivity (S_{CO}, %) were calculated according to the following equation:

$$X_{CO_2}(\%) = 100 \times \left(1 - \frac{C_{CO_2,out} \times C_{N_2,in}}{C_{CO_2,in} \times C_{N_2,out}}\right)$$

$$S_{CO}(\%) = 100 \times \left(\frac{C_{CO}}{C_{CO} + C_{CH_4}}\right)$$

$$S_{CH_4}(\%) = 100 \times \left(\frac{C_{CH_4}}{C_{CO} + C_{CH_4}}\right)$$

3. Results and discussion

MIL-68(In) was chosen as a template for the preparation of the catalyst and was synthesized according to the reported method.[28,29] As shown in Fig. S1a,† all characteristic diffraction peaks of the as-prepared MIL-68(In) were in good agreement with those of the simulated MIL-68(In), demonstrating the pure phase, as confirmed by powder X-ray diffraction (PXRD). The N_2 adsorption results of as-prepared MIL-68(In) exhibited a type I isotherm, indicating the presence of microporosity and a calculated surface area of 1192 m^2 g^{-1} (Fig. S1b†). The SEM image of the as-prepared MIL-68(In) (Fig. S1d†) illustrated a hexagonal prism-shaped morphology, with an average length of 3.4 ± 4.6 μm and an average diameter size of 0.6 ± 0.3 μm (Fig. S1e and f†). In order to obtain the carbon-based materials, MIL-68(In) was carbonized under a N_2 and/or N_2/H_2O (steam-pyrolysis) atmosphere at 600 °C for 6 h. Steam partial pressures of 0.86, 3.13, and 7.28 kPa were controlled by setting the bubbler temperatures to 5, 25 and 40 °C, respectively.[27] The resulting samples were denoted as In@C for the sample pyrolyzed under N_2, and as In@C-5, In@C-25 and In@C-40 for the samples pyrolyzed under N_2/H_2O, where the number represents the bubbler temperature in celsius degrees. PXRD analysis, as illustrated in Fig. 1a, revealed that only the c-In_2O_3 crystalline phase was formed after both the pyrolysis and steam-pyrolysis treatments. No additional peaks associated with MIL-68(In) were observed in the XRD patterns, indicating complete decomposition of MIL-68(In). Furthermore, it was found that the steam partial pressure has no influence on the phase composition (see Table S2†).

Transmission Electron Microscopy (TEM) was conducted to elucidate the morphological differences between the pyrolyzed (In@C) and steam-pyrolyzed (In@C-*X*) samples. As depicted in Fig. 1c, the In@C sample retained the rod-like morphology characteristic of MIL-68(In), indicating highly dispersed metal oxide nanoparticles encapsulated within a porous graphitic carbon matrix. For the steam-pyrolyzed In@C-5 sample, the rod-like structure was similarly preserved (Fig. S2d and e†), indicating that a steam partial pressure of 0.86 kPa is insufficient to alter the original MOF morphology. Conversely, Fig. 1f and S2j and k† revealed the absence of rod-like structures in the In@C-25 and In@C-40 samples. Moreover, the In@C-25 sample showed a reduced carbon amount, while the In@C-40 sample exhibited almost no presence of carbon, suggesting that the initial MOF morphology decomposes during steam pyrolysis due to the partial gasification of the carbon matrix. Additionally, the In@C and In@C-5 samples displayed a bimodal particle size distribution, as shown in Fig. S2c and f.† The smaller particles were confined within the carbon matrix, likely due to carbon encapsulation that limits particle growth. Larger particles were observed at the matrix edges, indicating reduced confinement in these regions. Notably, when the steam content was increased to 3.13 kPa (In@C-25), a more uniform distribution with an average particle size of 19.8 nm was obtained, attributed to enhanced gasification of the carbon matrix (Fig. S2i†). However, further increasing the steam content to 7.28 kPa (In@C-40) led to a larger average particle size of 24.5 nm, suggesting that excessive steam could over-gasify the carbon matrix, promoting particle agglomeration (Fig. S2l†). These findings suggest that a moderate steam partial pressure (around 3.13 kPa) optimizes particle size distribution by balancing carbon gasification

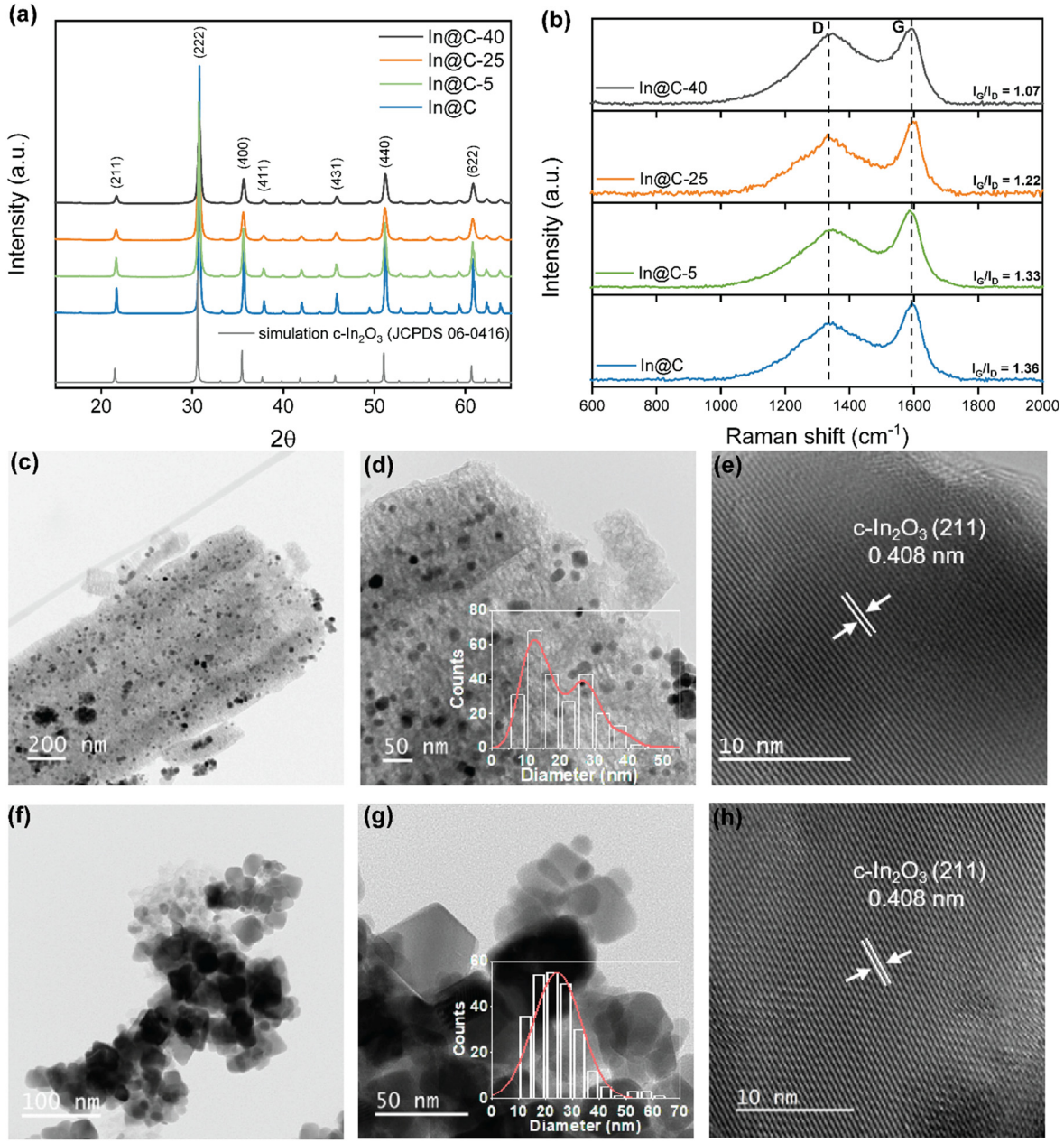

Fig. 1 a) PXRD patterns of In@C, In@C-5, In@C-25, In@C-40, and simulated c-In_2O_3. b) Raman spectra of In@C, In@C-5, In@C-25, and In@C-40. TEM image of In@C c) at low magnification and particle size distribution (inset) d) at high magnification e) interplanar distance corresponding to the lattice distance of (211) plane of In_2O_3. TEM image of In@C-25 f) at low magnification and particle size distribution (inset) g) at high magnification h) interplanar distance corresponding to the lattice distance of (211) plane of In_2O_3.

and minimizing excessive particle coalescence. High-magnification TEM images (Fig. 1e and h) allowed for the measurement of lattice spacings of 0.408 nm for In@C and In@C-25, which are consistent with the *d*-spacing of the (211) plane of c-In_2O_3. Furthermore, STEM coupled with EDX in Fig. S3† revealed that the In_2O_3 nanoparticles are well-distributed on the rod-like carbon matrix, confirming the confinement of In_2O_3 within the graphitic carbon matrix in the In@C sample. In contrast, in the steam-pyrolyzed In@C-25 sample, the carbon matrix is no longer visible due to partial oxidation, resulting in a significantly reduced carbon content. Consequently, the remaining carbon is homogeneously distributed on the surface of the In_2O_3 particles, as evidenced in Fig. S4.† Overall, all these results corroborate that while the introduction of water into the N_2 flow does not alter the phase composition, it markedly transforms the morphology of the carbon matrix used as a support. Next, we conducted thermogravimetric analysis (TGA) to determine the amount of carbon in the In@C and In@C-*X* solids. As shown in Fig. S5,† the weight loss decreased with the increase in steam partial pressure in the N_2 flow. Specifically, weight losses of 22.0%, 12.2%, 6.5% and

5.3% were observed for In@C, In@C-5, In@C-25 and In@C-40, respectively. These findings confirm that the presence of water serves as an oxidizing agent, leading to the partial gasification of carbon during the pyrolysis process, and they align with those observed by STEM.[27] Additionally, these results are consistent with the N_2 adsorption measurements (Fig. S6†). We observed a decrease in the BET-specific surface area with the reduction of carbon content: 212, 173, 127, and 91 $m^2\ g^{-1}$ for In@C, In@C-5, In@C-25 and In@C-40, respectively (Table S1†).

The UV-vis-NIR absorption spectra of the In@C-*X* and pristine In_2O_3 samples were measured to determine their light-harvesting properties. Due to the characteristics of carbon-based materials, the In@C-*X* samples exhibited stronger light absorption compared to pristine In_2O_3, particularly in the visible and NIR light range, as illustrated in Fig. S7,† suggesting high solar energy utilization efficiency and indicating the potential for enhanced photothermal and photochemical activity.[21,24]

Raman spectroscopy was utilized to further understand the degree of graphitization in the carbon matrix and the defects in the indium oxide lattice. The Raman spectra of the materials exhibited the characteristic vibration bands of disordered graphite (D band) at 1340 cm^{-1} and the E_{2g} mode of graphite (G band) at 1590 cm^{-1}.[30] The intensity ratio of the two bands (I_G/I_D) was used to evaluate the graphitization degree of the different samples. We found that the higher steam content in the N_2 flow during pyrolysis, the lower graphitization degree of the carbon matrix (1.36 for In@C, 1.33 for In@C-5, 1.22 for In@C-25 and 1.07 for In@C-40) (Fig. 1b). Moreover, the defective sites in the indium oxide lattice were also investigated using Raman spectroscopy. Fig. S8a† showed peaks at approximately 126 and 297 cm^{-1}, attributed to the In–O vibrations within InO_6 octahedra. The peak near 357 cm^{-1} corresponds to the stretching vibrations of In–O–In, indicative of unsaturated lattice oxygen (InO_{6-x}).[31] Additionally, Fig. S8b† presented the relative peak intensity ratio between unsaturated InO_{6-x} (357 cm^{-1}) and saturated InO_6 (126 cm^{-1}). Notably, the increased ratio observed in the In@C-25 and In@C-40 samples, compared to In@C, suggests that the steam-pyrolysis process effectively enhances the concentration of oxygen vacancies in In_2O_3. Conversely, In@C-5 exhibited a similar ratio to the In@C sample, implying that sufficient water content is required for the formation of oxygen vacancies.

To further demonstrate the generation of oxygen vacancies through the steam-pyrolysis treatment, X-ray photoelectron spectroscopy (XPS) measurements were performed in the In@C sample together with the In@C-25 catalyst as representative of the steam-pyrolyzed samples. With respect to the In3d core level, both samples showed the characteristic $In3d_{5/2}$ and $In3d_{3/2}$ peaks located at 444.6 and 452.1 eV, respectively, in good agreement with the peak-to-peak gap of 7.6 eV attributable to indium oxide (Fig. 2a and d).[32] When it comes to the O1s core level, the spectra of both samples could be deconvoluted into 4 peaks centered at 530.1, 530.7, 532.3 and 533.7 eV corresponding to lattice oxygen, defect-related oxygen species, surface –OH groups and C=O, respectively (Fig. 2b and e).[33–35] However, the relative contribution of the component ascribed to oxygen defects was markedly higher in the case of the In@C-25 catalyst, achieving 35.3% in comparison to the 27.5% for the In@C sample. This clearly indicates that the introduction of steam during the pyrolysis induces the generation of defects in the

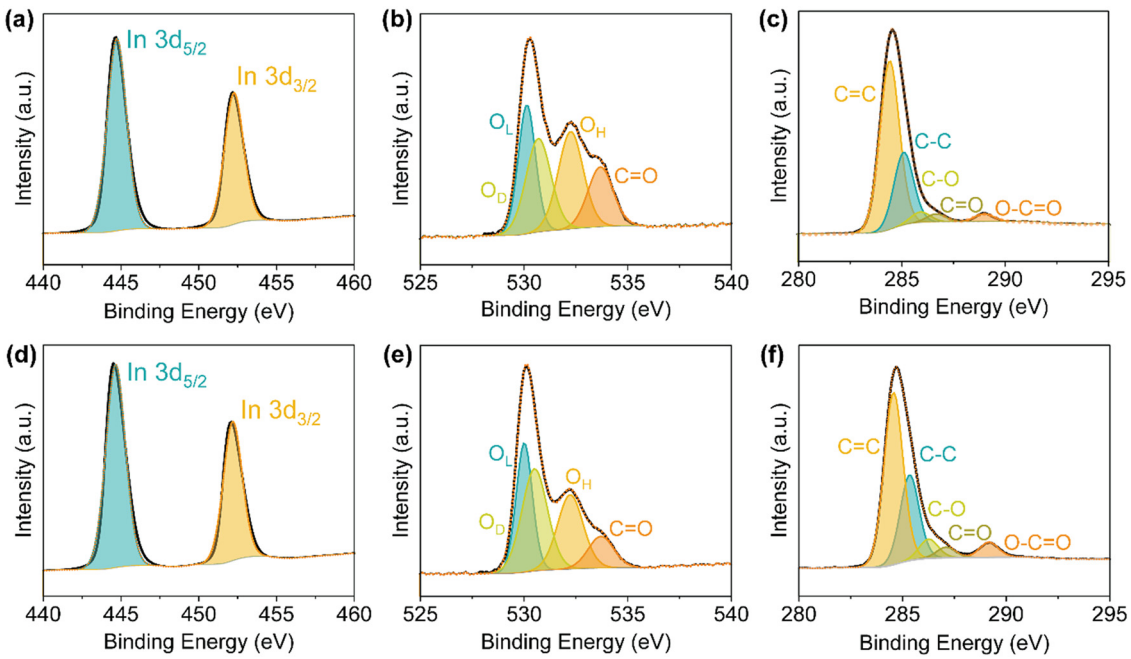

Fig. 2 XPS measurements of (a)–(c) In@C sample and (d)–(f) In@C-25 sample.

indium oxide lattice, in line with the Raman measurements above. Furthermore, analysis of the C1s core level of the In@C catalyst revealed the presence of five distinct components located at 284.4, 285.1, 285.9, 286.7 and 289.0 eV that can be ascribed to C=C (sp^2), C–C (sp^3), C–O, C=O and O–C=O species, respectively.[36] It is worth noting that in this case the relative contribution of the graphitic carbon (sp^2) component accounted for 62.7%. In the In@C-25 sample, however, the sp^2 component achieved 56.8%, thus indicating a lower degree of graphitization for the steam-pyrolyzed samples. These observations are, again, in good agreement with the Raman results that suggested a lower degree of graphitization when the pyrolysis of the MOF is performed in the presence of steam.

The catalytic performance of all In@C and In@C-*X* samples for the reverse water-gas shift (RWGS) reaction was investigated using a 300 W Xe lamp at a light intensity of 3.3 W cm^{-2} under continuous flow configuration. It is well-established that alkali promoters can enhance the strength of CO_2 adsorption and increase the CO_2 adsorption capacity. Therefore, we initially selected three different alkali promoters (K, Rb, Cs) to impregnate into the In@C and In@C-*X* samples, as previously described, and to study their catalytic performance in the photothermal RWGS reaction. The loading amount of each alkali promoter was set at 2 wt%. According to the PXRD patterns (Fig. S9†), no peaks corresponding to the loaded promoters were observed, indicating that the promoters were well-dispersed within the catalysts after wet impregnation. To optimize the promoter for the RWGS reaction, alkali-promoted In@C/In@C-25 and pure In@C/In@C-25 catalysts were evaluated for their photothermal CO_2 hydrogenation performance. As depicted in Fig. S10a and c,† the catalytic activity for CO_2 hydrogenation was significantly enhanced by the impregnation of alkali promoters, whereas the pure In@C and pure In@C-25 samples exhibited almost no activity. Additionally, all alkali-promoted catalysts displayed significantly higher surface temperatures compared to the pure samples, indicating that alkali promoters improve photothermal performance by increasing the catalyst

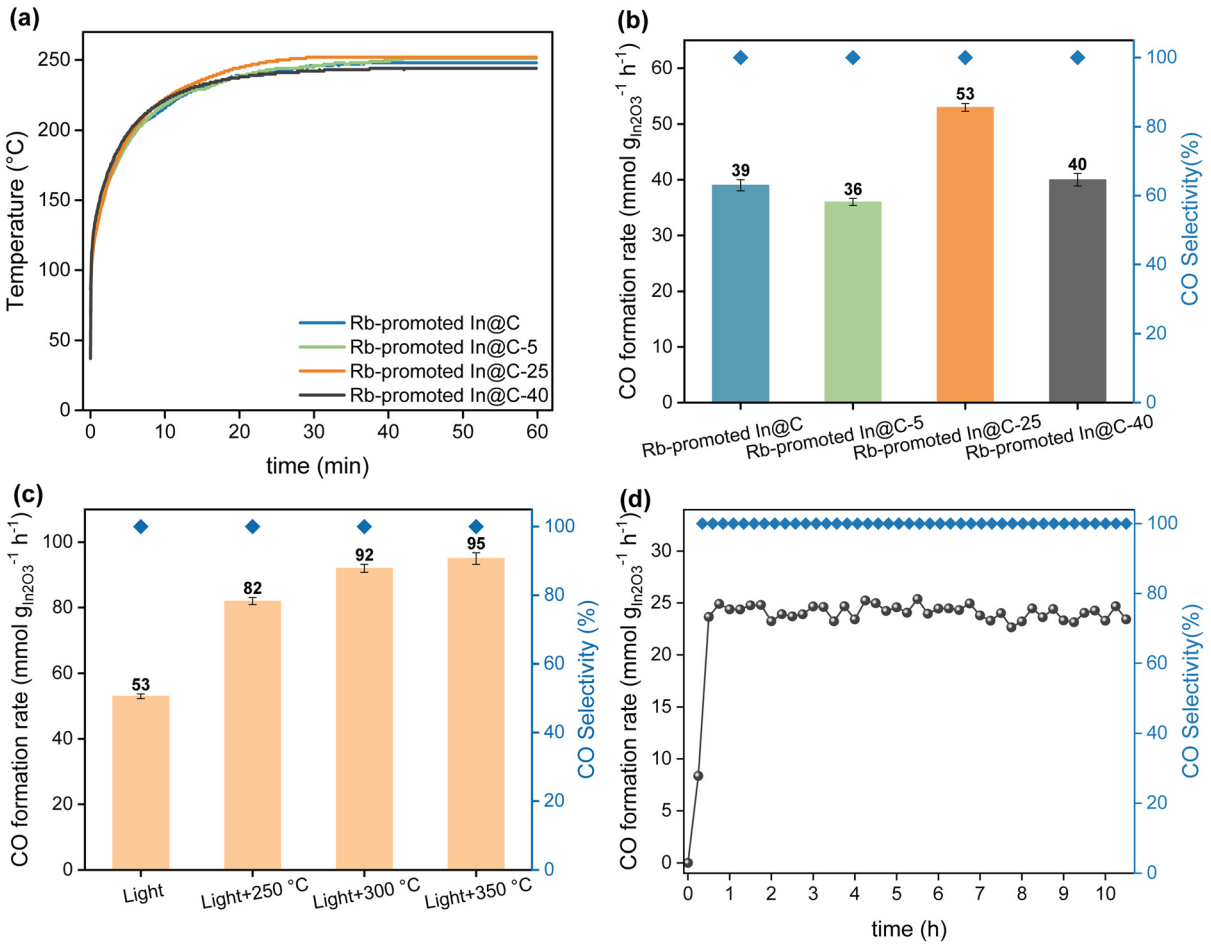

Fig. 3 a) Temperature evolution over Rb-promoted In@C/In@C-*X* catalysts under 3.3 W cm^{-2} light irradiation. b) CO production rate and CO selectivity over Rb-promoted In@C/In@C-*X* catalysts without external heating under irradiation of 3.3 W cm^{-2}. Reaction conditions: GSHV = 20 000 mL h^{-1} g^{-1}, 1 bar. c) CO production rate and CO selectivity over Rb-promoted In@C-25 at different temperatures under irradiation of 3.3 W cm^{-2}. Reaction conditions: GSHV = 20 000 mL h^{-1} g^{-1}, 1 bar. d) Stability test of Rb-promoted In@C-25 without external heating at 3 W cm^{-2}. Reaction conditions: GSHV = 20 000 mL h^{-1} g^{-1}, 1 bar.

temperature (Fig. S10b and d†). The Rb promoter exhibited remarkable catalytic activity in both the In@C and In@C-25 samples, which can be attributed to the synergistic geometric and electronic effects of Rb. Electronically, the activity sequence of alkali promoters follows the order Cs > Rb > K, closely matching the electropositivity of the element.[37] Geometrically, however, the ionic radii follow the order K < Rb < Cs, indicating that larger alkali metal ions may hinder reactant adsorption on the catalyst surface, particularly in porous materials. Considering both geometric and electronic factors, Rb emerges as the optimal promoter, exhibiting superior catalytic performance.[38] Consequently, Rb was selected as the most effective promoter for enhancing photothermal catalytic CO_2 hydrogenation.

The photothermal catalytic CO_2 hydrogenation reaction of Rb-promoted In@C/In@C-*X* catalysts under various pyrolysis conditions was then evaluated. As shown in Fig. 3a, all samples exhibited a progressive increase in temperature upon light irradiation, stabilizing after approximately 15 minutes, with all Rb-promoted catalysts reaching a similar surface temperature of around 250 °C. Fig. 3b demonstrated the CO production rate and CO selectivity of the Rb-promoted catalysts under different pyrolysis conditions. Notably, the Rb-promoted In@C-25 exhibited the highest catalytic performance, achieving a CO production rate of 53 mmol $g_{In_2O_3}^{-1}$ h^{-1}, which is nearly 40% higher than that of the Rb-promoted In@C catalyst. To the best of our knowledge, this performance surpasses that of current state-of-the-art indium-based catalysts for photo-thermal CO_2 hydrogenation under continuous flow configuration (Table S8†). Furthermore, no catalytic activity was observed in commercial Rb-promoted In_2O_3, further highlighting the beneficial effect of steam pyrolysis in enhancing catalytic performance (Fig. S11†). Oxygen-vacancy-enriched materials have been reported to potentially improve the light-harvesting properties and enhance the photothermal catalytic activity.[19,20,39] Indeed, our XPS and Raman spectroscopy results revealed that the steam-pyrolysis process generates additional oxygen vacancies on the catalyst surface when the steam partial pressure exceeds 3.13 kPa. Therefore, we hypothesize that the superior catalytic performance of the Rb-promoted In@C-25 sample is attributable to the increased oxygen vacancies, which improve CO_2 adsorption capacity and H_2 dissociation ability, as we will discuss below. Conversely, the lack of performance improvement in the Rb-promoted In@C-5 sample suggests that insufficient steam partial pressure did not generate significant defect sites. Additionally, the lower CO production rate observed for the Rb-promoted In@C-40 is likely due to its reduced specific surface area (Table S1†) and larger particle size (Fig. S2f†).

To gain deeper insights into the differences in catalytic performance between pyrolysis and steam-pyrolysis, we conducted additional characterizations. The In@C-25 catalyst was selected for further study as the representative steam-pyrolysis sample due to its superior catalytic performance. CO_2-TPD measurements were performed to evaluate the CO_2 adsorption/desorption capability on the catalyst surface (Fig. S12†). No significant CO_2 adsorption was observed in the pure In@C-25. In contrast, Rb impregnation significantly enhanced CO_2 adsorption, as evidenced by stronger peak intensities and higher desorption temperatures, indicating improved CO_2 adsorption capacity and a stronger interaction between CO_2 and the catalyst. Furthermore, Rb-promoted In@C-25 exhibited higher peak intensities at approximately 100 °C and 300 °C compared to Rb-promoted In@C, which are associated with physically adsorbed CO_2 and the decomposition of bicarbonate (HCO_3^-) and carbonate (CO_3^{2-}) species, respectively.[40,41] One of the explanations for the enhanced CO_2 adsorption ability of Rb-promoted In@C-25 could be the formation of surface oxygen defects introduced during steam-pyrolysis, as corroborated by XPS results. These oxygen defects facilitate the formation of bicarbonate species (HCO_3^-) during CO_2 adsorption.[42] This hypothesis is further supported by the more intense water peak (m/z = 18) observed around 300 °C for Rb-promoted In@C-25, corresponding to bicarbonate decomposition (see Fig. S12b†).

Additionally, H_2-TPR measurements were conducted to evaluate the reduction temperatures of the catalysts. As illustrated in Fig. S13,† the first peak at approximately 200–300 °C is attributed to the reduction of surface In_2O_3, while the progressively increasing signal above 500 °C corresponds to the reduction of bulk In_2O_3. Notably, Rb-promoted In@C-25 exhibited surface reduction temperatures at 228 °C and 276 °C, which are 30 °C and 39 °C lower than those observed for Rb-promoted In@C, respectively. These lower surface reduction temperatures are due to the presence of defective sites formed during steam-pyrolysis, which facilitate H_2 dissociation on the catalyst surface and result in lower reduction temperatures.[43] Overall, the oxygen vacancies introduced by steam-pyrolysis could enhance the CO_2 adsorption and H_2 dissociation capacities of indium oxide, consistent with the improved catalytic performance observed in the photothermal CO_2 hydrogenation reaction.

Given the endothermic nature of the RWGS reaction, which benefits from higher reaction temperatures, we further investigated the catalytic performance of Rb-promoted In@C-25 samples within a temperature range of 250 to 350 °C. To achieve these temperatures, which are limited by the maximum irradiance of the lamp, we installed an external heater at the bottom of the catalyst bed. As shown in Fig. 3c, applying external heating at 250 °C significantly enhanced catalytic performance compared to without external heating, achieving a CO production rate of 82 mmol $g_{In_2O_3}^{-1}$ h^{-1} and 100% CO selectivity. However, increasing the external heating from 250 °C to 350 °C resulted in only a slight improvement in CO production. This suggests that the photochemical effect diminishes as external temperatures increase. The detailed mechanism behind this observation will be discussed further below. Noted here that all catalysts demonstrated exceptional CO selectivity across the entire range of reaction temperatures. Considering the impressive catalytic performance of Rb-promoted In@C-25, we assessed

its long-term stability under the reaction conditions. As illustrated in Fig. 3d, the catalyst demonstrated exceptional robustness, with no significant decline in CO_2 conversion or CO selectivity over 10 hours of continuous reaction.

Although from the thermodynamics point of view, the RWGS reaction is not particularly favored under high pressure, these operating conditions offer significant industrial advantages such as higher production capacity per unit volume and therefore higher efficiency.[44–46] Furthermore, high pressures also eliminate the need for pre-depressurization and subsequent compression for potential Fischer–Tropsch synthesis. For these reasons, we studied the impact of pressure on the catalytic activity of Rb-promoted In@C-25 samples. Fig. S14† shows the CO production rate and CO selectivity of the Rb-promoted In@C-25 catalyst at 10 bar across different temperatures. Without external heating, the CO production rate at 10 bar was 41 mmol $g_{In_2O_3}^{-1}$ h^{-1}, significantly lower than at 1 bar due to the increased thermal conductivity and convective cooling which decreased the surface temperatures at higher pressures (Table S4†).[47,48] However, external heating mitigated this effect, aligning surface temperatures at 10 bar with those at ambient pressure (Table S4†). Under external heating conditions (250–350 °C), the photo-thermal performance at 10 bar improved significantly. Notably, CO production rates reached 98 and 107 mmol $g_{In_2O_3}^{-1}$ h^{-1} at 250 °C and 300 °C, respectively, surpassing those at ambient conditions and setting a new benchmark for the photo-thermal RWGS reaction using indium-based catalysts in a continuous flow setup (Table S8†). Interestingly, despite methanation being favored under high H_2 partial pressure, our catalyst maintained near 100% selectivity towards CO, with no detectable methane formation. Nevertheless, our results also revealed a decrease in CO selectivity at 350 °C, accompanied by the emergence of methane as a by-product, probably due to the partial reduction of indium oxide and the formation of metallic indium, as evidenced by PXRD analyses of the samples after reaction (Fig. S15†). These findings suggest that both elevated temperatures and H_2-rich reaction mixtures compromise the stability of indium oxide, thereby altering the reaction pathway and favoring methane formation.[18]

In view of these results, we attribute the enhanced performance of the Rb-promoted In@C-25 catalyst to the steam-pyrolysis strategy that facilitates the generation of a defective indium oxide-carbon composite. On the one hand, the formation of defects on the indium oxide improves the CO_2 adsorption and H_2 dissociation capacities of the catalyst. On the other hand, the presence of carbon enhances the light harvesting properties and the light-to-heat conversion capabilities of the samples, therefore boosting the catalytic activity for the photo-thermal RWGS reaction.

4. Mechanistic study

To further elucidate the reaction mechanisms involved in the photo-thermal CO_2 hydrogenation by Rb-promoted In@C-25, we conducted a series of light intensity studies under both light and dark conditions. Under dark conditions, we applied a 1 mm thin layer of Ti_2O_3, a material known for its excellent light-to-heat conversion properties but inactivity in the RWGS reaction, on the catalyst surface.[49] This approach aimed to isolate the pure photo-chemical contribution while maintaining the same surface temperature profile as observed during direct illumination. As shown in Tables S6 and S7,† the surface temperatures of the catalyst covered with Ti_2O_3 closely matched those obtained under direct illumination. This suggests that the thin Ti_2O_3 layer provides comparable photo-thermal heating while effectively blocking pure photo-chemical effects.

As shown in Fig. 4a, the exponential dependence of the CO production rate on direct illumination intensity is a characteristic feature of thermally driven transformations, supporting a light-to-heat mechanism.[48] The large difference in CO production rate between dark and light conditions increases with higher light intensity, even when the surface temperature remains similar (Table S6†). At a light intensity of 3.3 W cm^{-2}, the CO production rate under indirect illumination is only 7 mmol $g_{In_2O_3}^{-1}$ h^{-1}, which is more than 7 times lower than under direct illumination. However, the CO production rates were very similar when the light intensity was below 2.52 W cm^{-2}. These observations suggest that non-thermal effects dominate the reaction pathway at high light intensities whereas thermal effects are preeminent at low irradiances. Moreover, Fig. 4b showed the CO production rates under direct and indirect illumination with external heating. The difference in CO production rate between direct and indirect illumination is reduced from 86.8 to 65.0% when external heating is increased to 300 °C (Table S7†). This indicates that the contribution of hot carriers, generated by the photo-excitation of Rb-promoted In@C-25, gradually diminishes with increasing reaction temperature, likely due to the recombination of charge carriers at elevated temperatures. Interestingly, both Fig. 4a and b showed that CO selectivity remains unaffected by either direct or indirect illumination, suggesting that hot carriers do not alter the reaction pathway. To provide a more comprehensive evaluation of the impact of light on the catalyst's performance, we determined the apparent activation energy (E_a) of CO_2 hydrogenation on Rb-promoted In@C-25 under both dark and light conditions, as shown in Fig. S16.† The apparent activation energy in the dark was 131 ± 7 kJ mol^{-1}, which was reduced to 110 ± 4 kJ mol^{-1} upon light irradiation. This reduction suggests that light-induced charge carriers can promote the activation of reactants, accelerating the reaction and enhancing the production rate.

To further investigate the photochemical properties, transient photocurrent measurements (Fig. S19†) and steady-state photoluminescence (PL) analysis (Fig. S20†) were performed on the Rb-promoted In@C/In@C-*X* samples, using commercial Rb-promoted In_2O_3 as a reference. Notably, the photocurrent increased with increasing carbon content, from Rb-promoted In@C-40 to Rb-promoted In@C, with Rb-

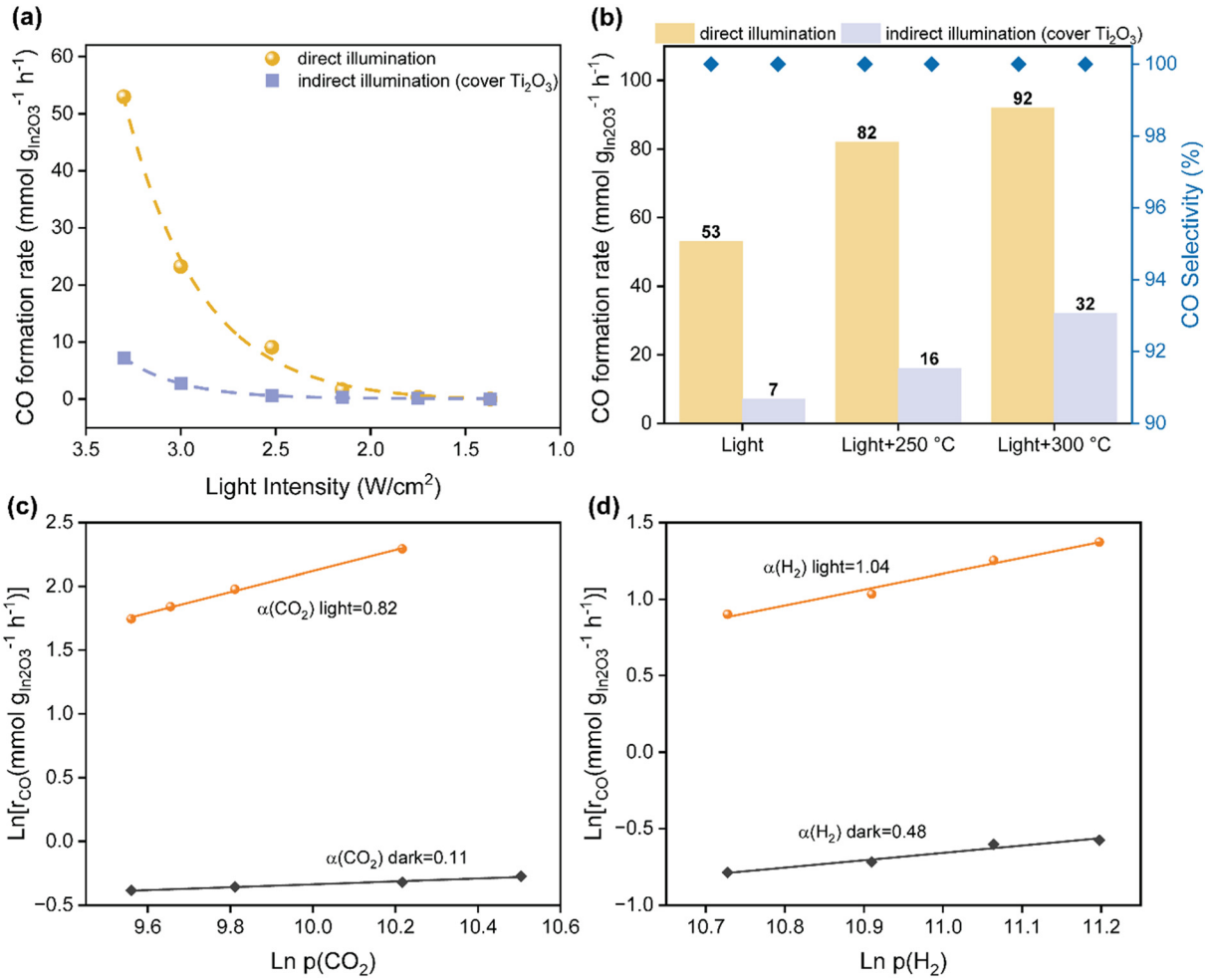

Fig. 4 a) Influence of light intensity on the CO_2 conversion over Rb-promoted In@C-25 catalyst under direct and indirect illumination without external heating. b) CO production rate and CO selectivity over Rb-promoted In@C-25 under direct and indirect illumination of 3.3 W cm^{-2} without and with external heating. c) Dependence of CO production rate on the partial pressures of CO_2 under 1.37 W cm^{-2} light irradiation (orange spheres) and dark conditions (grey diamond) over Rb-promoted In@C-25 with external heating of 250 °C. d) Dependence of CO production rate on the partial pressures of H_2 under 1.37 W cm^{-2} light irradiation (orange spheres) and dark conditions (grey diamond) over Rb-promoted In@C-25 with external heating of 250 °C. Reaction conditions: GSHV = 20 000 mL h^{-1} g^{-1}, 1 bar.

promoted In@C exhibiting the highest photocurrent. This result highlights that an increased amount of carbon could improve the charge separation and transfer efficiency of photogenerated electron–hole pairs.[50,51] However, the lower concentration of oxygen vacancies in the Rb-promoted In@C sample resulted in limited catalytic activity, suggesting a balance between carbon content and amount of oxygen vacancies to maximize the photo-thermal performance.[20] Meanwhile, weaker PL emissions were observed in Rb-promoted In@C/In@C-*X* samples compared to commercial Rb-promoted In_2O_3, indicating charge transfer from In_2O_3 to the carbon. Overall, these photochemical studies demonstrate that the incorporation of carbon not only enhances light-harvesting properties but also improves charge separation and transfer efficiency.

To further confirm the influence of photo-generated charge carriers on the reaction mechanism, we estimated the reaction orders of CO_2 and H_2 under both light illumination and dark conditions, since these parameters are generally independent on temperature and are directly related to the reaction pathway (Fig. 4c and d). Under dark conditions, the reaction order of H_2 was found to be 0.48, and it increased to 1.04 upon light irradiation. According to the Hougen–Watson type models, a reaction order less than 1 is typically indicative of surface species inhibition.[50,51] The lower H_2 reaction order indicates the competitive adsorption between hydrogen and other surface species, such as CO_2 or reaction intermediates, that hinders the availability of active sites for hydrogen adsorption and dissociation. Upon light irradiation, the H_2 reaction order increased significantly to 1.04, indicating a strong dependence of the reaction rate on hydrogen concentration. This shift suggests that light irradiation not only enhances hydrogen adsorption but also mitigates the inhibiting effects of surface species. As for CO_2, the reaction order transitioned from 0.11 under dark conditions to 0.82 upon light irradiation. The near-zero

reaction order in the dark suggests that the reaction rate is largely independent on the CO_2 concentration, which could be indicative of a saturated CO_2 adsorption site or a kinetically slow CO_2 activation process. Upon light illumination, the dramatic increase in the CO_2 reaction order to 0.82 highlights the activation of CO_2 as a key step in the photothermal process. This increase suggests that the photothermal process enhances the adsorption and activation of CO_2 on the catalyst surface, making CO_2 concentration more critical for the reaction rate under illuminated conditions.

Finally, additional experiments were conducted to evaluate the influence of the irradiation wavelength on the catalytic activity of the In@C-25 catalyst. To this end, we evaluated the catalytic performance under full-spectrum radiation and using a UV cut-off filter ($\lambda > 420$ nm) both under the same light intensity. As shown in Fig. S17,† the CO production rate under full spectrum was slightly higher than that obtained using the UV filter, thus indicating that visible and IR photons are the main responsible for the catalytic activity, although UV radiation exhibits a certain contribution through pure photochemical effects.

5. Conclusion

In summary, we have successfully developed an effective and selective Rb-promoted MOF-derived indium oxide catalyst *via* steam-pyrolysis for photothermal CO_2 hydrogenation. Notably, the Rb-promoted In@C-25 catalyst exhibited exceptional catalytic performance in the photothermal RWGS reaction, achieving 53 mmol $g_{In_2O_3}^{-1}$ h^{-1} CO production rate with a 100% selectivity. Comprehensive characterization results revealed that the appropriate bubbler temperature during the steam-pyrolysis is crucial for generating the defective sites on the catalyst surface while maintaining high porosity. Mechanistic investigations highlighted that the reaction mechanism follows a non-thermal pathway, particularly at high irradiances, in combination with pure thermal effects. Overall, this novel method could provide a pathway to more efficient and sustainable photothermal CO_2 hydrogenation, reinforcing the promise of steam-pyrolyzed MOF-derived materials for future carbon-neutral fuel production.

Data availability

The data supporting this article have been included as part of the ESI.†

Conflicts of interest

There are no conflicts to declare.

Acknowledgements

We gratefully acknowledge the financial support from King Abdullah University of Science and Technology (KAUST).

References

1 V. Bhoi, R. Naidu and A. Bera, in *Advances and Technology Development in Greenhouse Gases: Emission, Capture and Conversion*, Elsevier, 2024, pp. 19–38.
2 C. Mohan, J. Robinson, L. Vodwal and N. Kumari, in *Green Chemistry Approaches to Environmental Sustainability*, Elsevier, 2024, pp. 357–374.
3 Y. Zhu, S. Wu, J. Li, Q. Jia, T. Zhang, X. Zhang, D. Han and Y. Tan, *J. Energy Storage*, 2024, **83**, 110663.
4 N. Yusuf, F. Almomani and H. Qiblawey, *Fuel*, 2023, **345**, 128178.
5 P. Maksimov, A. Laari, V. Ruuskanen, T. Koiranen and J. Ahola, *Chem. Eng. J.*, 2021, **418**, 129290.
6 A. Kaithal, C. Werlé and W. Leitner, *JACS Au*, 2021, **1**, 130–136.
7 P. R. Ellis, D. I. Enache, D. W. James, D. S. Jones and G. J. Kelly, *Nat. Catal.*, 2019, **2**, 623–631.
8 A. Ramirez, L. Gevers, A. Bavykina, S. Ould-Chikh and J. Gascon, *ACS Catal.*, 2018, **8**, 9174–9182.
9 Y. Wang, Y. Liu, L. Tan, X. Lin, Y. Fang, X. F. Lu, Y. Hou, G. Zhang and S. Wang, *J. Mater. Chem. A*, 2023, **11**, 26804–26811.
10 M. Ahmadi Khoshooei, X. Wang, G. Vitale, F. Formalik, K. O. Kirlikovali, R. Q. Snurr, P. Pereira-Almao and O. K. Farha, *Science*, 2024, **384**, 540–546.
11 H.-X. Liu, S.-Q. Li, W.-W. Wang, W.-Z. Yu, W.-J. Zhang, C. Ma and C.-J. Jia, *Nat. Commun.*, 2022, **13**, 867.
12 D. Mateo, J. L. Cerrillo, S. Durini and J. Gascon, *Chem. Soc. Rev.*, 2021, **50**, 2173–2210.
13 D. Mateo, N. Morlanes, P. Maity, G. Shterk, O. F. Mohammed and J. Gascon, *Adv. Funct. Mater.*, 2021, **31**, 2008244.
14 C. Guo, Y. Tang, Z. Yang, T. Zhao, J. Liu, Y. Zhao and F. Wang, *ACS Nano*, 2023, **17**, 23761–23771.
15 M. Gao, J. Zhang, P. Zhu, X. Liu and Z. Zheng, *Appl. Catal., B*, 2022, **314**, 121476.
16 B. Deng, H. Song, Q. Wang, J. Hong, S. Song, Y. Zhang, K. Peng, H. Zhang, T. Kako and J. Ye, *Appl. Catal., B*, 2023, **327**, 122471.
17 Y. Peng, H. Szalad, P. Nikacevic, G. Gorni, S. Goberna, L. Simonelli, J. Albero, N. López and H. García, *Appl. Catal., B*, 2023, **333**, 122790.
18 X. Wang, J. Gallo, D. Mateo and J. Gascon, *J. Mater. Chem. A*, 2024, **12**, 23541–23550.
19 Y. Qi, L. Song, S. Ouyang, X. Liang, S. Ning, Q. Zhang and J. Ye, *Adv. Mater.*, 2020, **32**, 1903915.
20 Y. Qi, J. Jiang, X. Liang, S. Ouyang, W. Mi, S. Ning, L. Zhao and J. Ye, *Adv. Funct. Mater.*, 2021, **31**, 2100908.
21 L. Wang, Y. Dong, T. Yan, Z. Hu, F. M. Ali, D. M. Meira, P. N. Duchesne, J. Y. Y. Loh, C. Qiu, E. E. Storey, Y. Xu, W. Sun, M. Ghoussoub, N. P. Kherani, A. S. Helmy and G. A. Ozin, *Nat. Commun.*, 2020, **11**, 2432.
22 B. Han, Y. L. Zhang, Q. D. Chen and H. B. Sun, *Adv. Funct. Mater.*, 2018, **28**, 1802235.
23 I. S. Khan, L. Garzon-Tovar, D. Mateo and J. Gascon, *Eur. J. Inorg. Chem.*, 2022, **2022**, e202200316.

24 H. Zhang, T. Wang, J. Wang, H. Liu, T. D. Dao, M. Li, G. Liu, X. Meng, K. Chang and L. Shi, *Adv. Mater.*, 2016, **28**, 3703–3710.
25 I. S. Khan, D. Mateo, G. Shterk, T. Shoinkhorova, D. Poloneeva, L. Garzón-Tovar and J. Gascon, *Angew. Chem.*, 2021, **133**, 26680–26686.
26 J. Ma, J. Yu, G. Chen, Y. Bai, S. Liu, Y. Hu, M. Al-Mamun, Y. Wang, W. Gong and D. Liu, *Adv. Mater.*, 2023, **35**, 2302537.
27 I. S. Khan, L. Garzon-Tovar, T. Grell, G. Shterk, J. Cerrillo, T. Shoinkhorova, J. C. Navarro, F. Alahmadi, A. Sousa and A. Bavykina, *ACS Catal.*, 2023, **13**, 1804–1811.
28 R. Liang, L. Shen, F. Jing, W. Wu, N. Qin, R. Lin and L. Wu, *Appl. Catal., B*, 2015, **162**, 245–251.
29 C. Volkringer, M. Meddouri, T. Loiseau, N. Guillou, J. Marrot, G. Férey, M. Haouas, F. Taulelle, N. Audebrand and M. Latroche, *Inorg. Chem.*, 2008, **47**, 11892–11901.
30 S. Sänze and C. Hess, *J. Phys. Chem. C*, 2014, **118**, 25603–25613.
31 J. Gan, X. Lu, J. Wu, S. Xie, T. Zhai, M. Yu, Z. Zhang, Y. Mao, S. C. I. Wang and Y. Shen, *Sci. Rep.*, 2013, **3**, 1021.
32 I. N. Reddy, C. V. Reddy, M. Cho, J. Shim and D. Kim, *Mater. Res. Express*, 2017, **4**, 086406.
33 Z. M. Detweiler, S. M. Wulfsberg, M. G. Frith, A. B. Bocarsly and S. L. Bernasek, *Surf. Sci.*, 2016, **648**, 188–195.
34 W.-C. Chang, C.-H. Kuo, C.-C. Juan, P.-J. Lee, Y.-L. Chueh and S.-J. Lin, *Nanoscale Res. Lett.*, 2012, **7**, 1–7.
35 Z. Wan, Q. Mao and Q. Chen, *Chem. Eng. J.*, 2021, **403**, 126389.
36 L. Zhang, G. Chen, M. N. Hedhili, H. Zhang and P. Wang, *Nanoscale*, 2012, **4**, 7038–7045.
37 Q. Yang, V. A. Kondratenko, S. A. Petrov, D. E. Doronkin, E. Saraçi, H. Lund, A. Arinchtein, R. Kraehnert, A. S. Skrypnik and A. A. Matvienko, *Angew. Chem., Int. Ed.*, 2022, **61**, e202116517.
38 D. Li, N. Ichikuni, S. Shimazu and T. Uematsu, *Appl. Catal., A*, 1998, **172**, 351–358.
39 S. Cai, J. Chen, Q. Li and H. Jia, *ACS Appl. Mater. Interfaces*, 2021, **13**, 14221–14229.
40 K. Pokrovski, K. T. Jung and A. T. Bell, *Langmuir*, 2001, **17**, 4297–4303.
41 Y. Yang, Y.-X. Pan, X. Tu and C.-j. Liu, *Nano Energy*, 2022, **101**, 107613.
42 J. Yu, A. Muhetaer, Q. Li and D. Xu, *Small*, 2024, 2402952.
43 J. Ye, C. Liu, D. Mei and Q. Ge, *ACS Catal.*, 2013, **3**, 1296–1306.
44 L. Barberis, C. I. Versteeg, J. D. Meeldijk, J. A. Stewart, B. D. Vandegehuchte and P. E. de Jongh, *ACS Catal.*, 2024, **14**, 9188–9197.
45 R. M. Bown, M. Joyce, Q. Zhang, T. R. Reina and M. S. Duyar, *Energy Technol.*, 2021, **9**, 2100554.
46 E. Portillo, J. Gandara-Loe, T. Reina and L. Pastor-Pérez, *Sci. Total Environ.*, 2023, **857**, 159394.
47 L. Mascaretti, A. Schirato, T. Montini, A. Alabastri, A. Naldoni and P. Fornasiero, *Joule*, 2022, **6**, 1727–1732.
48 P. G. O'Brien, A. Sandhel, T. E. Wood, F. M. Ali, L. B. Hoch, D. D. Perovic, C. A. Mims and G. A. Ozin, *Adv. Sci.*, 2014, **1**, 1400001.
49 X. Li, H. O. Everitt and J. Liu, *Nano Res.*, 2019, **12**, 1906–1911.
50 A. A. Upadhye, I. Ro, X. Zeng, H. J. Kim, I. Tejedor, M. A. Anderson, J. A. Dumesic and G. W. Huber, *Catal. Sci. Technol.*, 2015, **5**, 2590–2601.
51 M. A. Vannice and W. H. Joyce, *Kinetics of catalytic reactions*, Springer, 2005.